HOSTED BY
ELSEVIER
CrossMark
Available online at www.sciencedirect.com
ScienceDirect
Water Science and Engineering 2015, 8(1): 68−77
http://www.waterjournal.cn

Experimental study on slope sliding and debris flow evolution with and without barrier

Ji-kun Zhao [a,b,*], Dan Wang [a], Jia-hong Chen [c]

[a] College of Engineering, Nanjing Agricultural University, Nanjing 210031, PR China
[b] Jiangsu Key Laboratory for Intelligent Agricultural Equipment, Nanjing Agricultural University, Nanjing 210031, PR China
[c] College of Civil Engineering, Tongji University, Shanghai 201804, PR China

Received 28 February 2014; accepted 9 September 2014
Available online 17 January 2015

Abstract

A constitutive model on the evolution of debris flow with and without a barrier was established based on the theory of the Bingham model. A certain area of the Laoshan Mountain in Nanjing, Jiangsu Province, in China was chosen for experimental study, and the slope sliding and debris flow detection system was utilized. The change curve of the soil moisture content was attained, demonstrating that the moisture content of the shallow soil layer increases faster than that of the deep soil layer, and that the growth rate of the soil moisture content of the steep slope is large under the first weak rainfall, and that of the gentle slope is significantly affected by the second heavy rainfall. For the steep slope, slope sliding first occurs on the upper slope surface under heavy rainfall and further develops along the top platform and lower slope surface, while under weak rainfall the soil moisture content at the lower part of the slope first increases because of the high runoff velocity, meaning that failure occurring there is more serious. When a barrier was placed at a high position on a slope, debris flow was separated and distributed early and had less ability to carry solids, and the variation of the greatest depth of erosion pits on soil slopes was not significant.

Keywords: Debris flow; Slope sliding; Geological disaster; Time domain reflectometry (TDR) technique; Detection system; Constitutive model

1. Introduction

Debris flow is a very destructive geological disaster. Loose material moves in response to debris flow's shearing force, thereby creating a secondary disaster induced by erosion. Rainfall is the main reason for slope instability, which leads to large-scale landslides. Current research on processes of debris flow always focuses on numerical simulation and experiments (Yair and Klein, 1973−1974; Hottan and Ohta, 2000; Magnus and Oliver, 2012). Nicholas et al. (2014) analyzed seven debris flows initiated in proglacial gullies. Gartner et al. (2014) used multiple regressions to develop models for predicting volumes of sediment. Setting a barrier is an effective measure of controlling the process of debris flow. Based on the simulation and experiments, many scholars (Mancarella et al., 2012; Brighenti et al., 2013) discussed the barrier's effect on debris flow evolution. Salciarini et al. (2010) used the discrete element method to assess the effectiveness of earthfill barriers. Mancarella et al. (2012) studied barrier effects and their possible role in infiltration processes and slope stability. They have found that debris flow was separated when it went through a barrier, and the barrier's position and rotation angle could change the deposition areas. Time domain reflectometry (TDR) is an electrical measurement technique used to determine the spatial location and nature of various objects (Robert, 2009; Suits et al., 2010; Ragni et al., 2012). Research on the use of the TDR detection technology in monitoring geological disasters began

This work was supported by the National Natural Science Foundation of China (Grant No. 51275250), the Natural Science Foundation of Jiangsu Province (Grant No. BK2010457), and the Agricultural Machinery Foundation of Jiangsu Province (Grant No. GXZ14003).
* Corresponding author.
E-mail address: jikunzhao_2006@163.com (Ji-kun Zhao).
Peer review under responsibility of Hohai University.

http://dx.doi.org/10.1016/j.wse.2015.01.003

in the mid-1990s (Dowding and Pierce, 1994). Pastuszka et al. (2014) determined the impact of the location of TDR probes in soil samples on moisture measurement. Results from some studies showed that TDR detection technology was valid for landslide monitoring (Liang et al., 2005). According to analysis of laboratory tests and field data, scholars have proposed a landslide monitoring method based on this technique, for example, Chen et al. (2009) measured the dielectric constant in highly conductive soils based on surface reflection coefficients.

In summary, real-time monitoring of landslides can be achieved using the TDR technology. However, results are mostly empirical. The scope of applicability of the regression formula needs further validation. Research on debris flow is difficult due to its sophisticated composition and the variability of dynamic processes. Studies that combine the constitutive theory of the erosion process with laboratory tests are few. Research on technology for detection of geological disasters can help to obtain related information and shed light on the process of slope sliding and evolution of debris flow.

In order to explore the process of slope failure under the influence of rainfall, a rainfall-controlled slope model was built based on the geological data of a certain area of the Laoshan Mountain in Nanjing, Jiangsu Province, in China, and a constitutive model of evolution of debris flow under the influence of barriers based on the theory of the Bingham model was also established. The rationality of the constitutive model was validated with experimental results and inversion analysis.

2. Establishment of constitutive model of debris flow evolution

The turbulence power of debris flow can be ignored because of high viscosity. Thus, the simplified Bingham model can be adopted:

$$\tau = \tau_B + \eta \frac{dv}{dy} \tag{1}$$

where τ is the shear strength, τ_B is the yield strength, η is the coefficient of viscosity, and dv/dy is the speed gradient in the y direction (the positive direction is downward). The Manning equation is used in the formula; the initial speed is (Han et al., 2012)

$$v_0 = 1.62 \left[\frac{S_v(1-S_v)}{d_{10}}\right]^{\frac{2}{3}} h^{\frac{1}{3}} \beta^{\frac{1}{6}} \tag{2}$$

where S_v is the volumetric concentration, d_{10} is the lower limit of particle size, h is the depth of mud, and β is the gradient of the slope. This formula has been verified with the measured data from the Jiangjia Gully and Hunshui Gully.

2.1. Constitutive model of debris flow erosion without barrier

Debris flow is affected by friction resistance and internal viscous forces. The slope surface resistance and mass of debris flow at time t_i can be written as

$$\begin{cases} f_i = \mu_0 \left(m_{i-1} + \dfrac{dm}{dt}\Delta t\right) g\cos\beta \\ m_i = m_{i-1} + \dfrac{dm}{dt}\Delta t \end{cases} \tag{3}$$

where f_i and m_i are the slope surface resistance and mass of debris flow at t_i, respectively; μ_0 is the friction coefficient of the slope surface; dm/dt is the change ratio of the mass of debris flow; g is the acceleration of gravity; and Δt is the time interval, where $\Delta t = t_i - t_{i-1}$.

The law of conservation of energy can be expressed as follows:

$$\begin{cases} \dfrac{1}{2}m_{i-1}v_{i-1}^2 + m_{i-1}g(Y-y_{i-1}) - m_i g(Y-y_i) - \dfrac{1}{2}m_i v_i^2 = W_{fi} + W_{si} \\ W_{fi} = \mu_0 g\cos\beta \displaystyle\int_{t_{i-1}}^{t_i} \left(m_{i-1} + \frac{dm}{dt}t\right) dt \end{cases} \tag{4}$$

where v_i is the velocity at t_i, Y is the initial height (relative to the ground) of debris flow, y_i is the decreasing height of debris flow at t_i, W_{fi} and W_{si} are the amounts of energy consumed in overcoming the slope surface resistance and viscous force from t_{i-1} to t_i, respectively.

Another expression of energy (Legros, 2002) at t_i is

$$E_i = h_{ci} + \frac{v_i^2}{2g} \tag{5}$$

where h_{ci} is the height of the center of mass of debris flow at time t_i. Then, the energy consumption of debris flow from t_{i-1} to t_i is

$$\Delta E_i = E_{i-1} - E_i = h_{ci-1} - h_{ci} + \frac{v_{i-1}^2 - v_i^2}{2g} \tag{6}$$

Combining Eq. (4) with Eq. (6) leads to the recursive expression Eq. (7) regarding v_i^2:

$$v_i^2 = \frac{v_{i-1}^2(m_{i-1}g - 1) + Am_{i-1} + B(dm/dt)\Delta t + C}{m_{i-1}g + g(dm/dt)\Delta t - 1} \tag{7}$$

where A, B, and C are expressed as $2g^2(y_i - y_{i-1})$, $2g^2(y_i - Y)$, and $2g(h_{ci} - h_{ci-1})$, respectively. The common expression of v_t^2 can be obtained:

$$v_t^2 = \frac{v_0^2(m_0 g - 1) + 2m_0 g^2 y_t + 2g^2(y_t - Y)(dm/dt)t + C_1}{m_0 g + g(dm/dt)t - 1} \tag{8}$$

where v_t and y_t are the velocity and decreasing height of debris flow at time t, respectively; C_1 is expressed as $2g(h_{ct} - h_{c0})$, where h_{c0} is the initial height of the center of mass of debris flow, and h_{ct} is the height of the center of mass of debris flow at time t; and m_0 is the initial mass of debris flow. A new equation of shear strength can be obtained by substituting the derivation of Eq. (8) into Eq. (1):

$$\tau = \tau_B + \eta \frac{m_t g^2}{(m_t g - 1)v_t} \tag{9}$$

where m_t is the mass of debris flow at time t.

2.2. Constitutive model of debris flow erosion with barrier

The barrier is designed as an equilateral triangular prism in order to simplify the calculation. It is sufficiently high and fixed on the central axis of the slope (Fig. 1). The distance from the vertex of the barrier to the top platform of the slope is x_1. The energy consumed by the debris flow in overcoming the friction when it flows through the barrier is ignored, because the effects of the barrier on shunting and obstructing are stronger than those on buffering.

According to the decomposition principle, as shown in Fig. 1, v_1 is decomposed into two symmetrical components at point e_1 at time t_1:

$$v_1' = \frac{v_1}{2\cos(\theta/2)} \tag{10}$$

where θ is the vertex angle of the barrier.

Similarly, the mass of debris flow has an equal distribution at time t_1:

$$m_1' = \frac{1}{2} m_1 \tag{11}$$

According to the law of conservation of energy, the velocity of the left body at point e_2 at time t_2 can be expressed as follows:

$$v_2'^2 = \frac{v_1'^2(m_1' g - 1) + Am_1' + B(\mathrm{d}m/\mathrm{d}t)(t_2 - t_1) + C}{m_1' g + g(\mathrm{d}m/\mathrm{d}t)(t_2 - t_1) - 1} \tag{12}$$

where A, B, and C are expressed as $2g^2(y_2 - y_1)$, $2g^2(y_2 - Y)$, and $2g(h_{c2} - h_{c1})$, respectively.

From e_2 to e_3, the trajectory of the debris flow is approximately a parabola. The resistance of the slope surface consists of longitudinal resistance and lateral resistance. The velocity of debris flow separating from the barrier at e_3 at time t_3 can be expressed as

$$v_3'^2 = \frac{v_2'^2(m_2' g - 1) + Am_2' + B(\mathrm{d}m/\mathrm{d}t)(t_3 - t_2) + C}{m_2' g + g(\mathrm{d}m/\mathrm{d}t)(t_3 - t_2) - 1} \tag{13}$$

where A, B, and C are expressed as $2g^2(y_3 - y_2)$, $2g^2(y_3 - Y)$, and $2g(h_{c3} - h_{c2})$, respectively.

The formula of the shear strength of the debris flow on the left side when it passes through the barrier can be obtained by substituting the derivation of Eq. (13) into Eq. (1):

$$\tau' = \tau_B + \eta \frac{m_t' g^2}{(m_t' g - 1)v_t'} \tag{14}$$

where m_t' can be expressed as $m_0/2 + (t - t_1/2)(\mathrm{d}m/\mathrm{d}t)$, and v_t' is the velocity at time t.

We can also rotate the barrier counterclockwise through an angle ϕ, as shown in Fig. 2. Assuming that the distance from the top platform of the slope to the vertex of the barrier is a fixed value x_1, the velocity v_1 at point e_1 at time t_1 will be decomposed into v_{L1} and v_{R1} when the debris flow reaches the vertex of the barrier. According to the sine theorem,

$$\frac{v_1}{|\sin(\pi - \theta)|} = \frac{v_{L1}}{|\sin(\theta/2 + \phi)|} = \frac{v_{R1}}{|\sin(\theta/2 - \phi)|} \tag{15}$$

where the subscripts L and R mean the left-side and right-side moving bodies. The mass of the moving body on the left side is not equal to that on the right side under the influence of rotation of the barrier. The masses on left and right sides after decomposition at point e_1 at time t_1 are

$$\begin{cases} m_{L1} = (m_1 - D)/2 \\ m_{R1} = (m_1 + D)/2 \end{cases} \tag{16}$$

where $D = \rho \tan\phi \int \mathrm{d}V$, in which ρ is the density of the debris flow, and V is the integration variable of volume.

According to the law of conservation of energy, the velocity of the left-side moving body at point e_3 at time t_3 can be obtained:

$$v_{L3}^2 = \frac{v_{L2}^2(m_{L2} g - 1) + Am_{L2} + B(\mathrm{d}m/\mathrm{d}t)(t_3 - t_2) + C}{m_{L2} g + g(\mathrm{d}m/\mathrm{d}t)(t_3 - t_2) - 1} \tag{17}$$

where A, B, and C are expressed as $2g^2(y_{L3} - y_{L2})$, $2g^2(y_{L3} - Y)$, and $2g(h_{Lc3} - h_{Lc2})$, respectively.

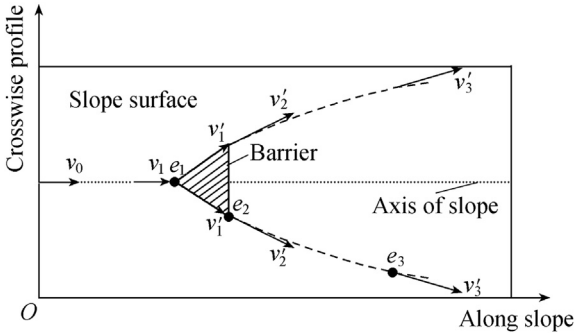

Fig. 1. Velocity diagram of debris flow with barrier on axis of slope surface.

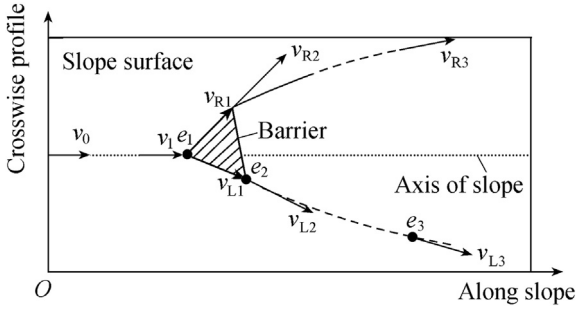

Fig. 2. Velocity diagram of debris flow with barrier rotating through an angle of ϕ.

An identical formula of the shear strength of the left-side moving body at time t can be expressed as follows:

$$\tau_L = \tau_B + \eta \frac{m_{Lt} g^2}{(m_{Lt} g - 1) v_{Lt}} \quad (18)$$

where m_{Lt} is $(m_0 - D)/2 + (t - t_1/2)\mathrm{d}m/\mathrm{d}t$.

Similarly, the shear strength of the right-side moving body at time t is

$$\tau_R = \tau_B + \eta \frac{m_{Rt} g^2}{(m_{Rt} g - 1) v_{Rt}} \quad (19)$$

where m_{Rt} can be expressed as $(m_1 + D)/2 + (t - t_1)\mathrm{d}m/\mathrm{d}t$.

3. Experimental design

3.1. Establishment of slope model

Fig. 3 shows the elevation contour of part of the area of the Laoshan Mountain. The mountain consists of bedrock on the bottom, the gravel layer, and the soil layer with a thickness ratio of about 3:2:9. Most of the area is steep, with gradients from 30° to 60°.

A slope model with two platforms, 4 m long, 2.1 m wide, and 2 m high, as shown in Fig. 4, was set up indoors. The model was a reduced-scale representation of the natural proportions of the soil structure with gradients from 30° to 45°. A bevel face with a thickness of 30 cm and a gradient of 5° was built on the bottom, and cement mortar was used to level it. It was considered the bedrock of the slope. The slope model consisted of a 20 cm-deep sand layer, a 90 cm-deep clay layer above the sand layer, a flat crest at its top, and a flat base near the slope toe. The platform of the slope was about 1 m long.

The soil was taken from the study area. In order to let the soil return to the pre-disturbance state, the slope model was allowed to stand full consolidation under natural conditions. Before the test, the initial values of monitoring indices were measured. After each index reached a relatively stable value, the experiments on slope sliding and debris flow erosion were performed.

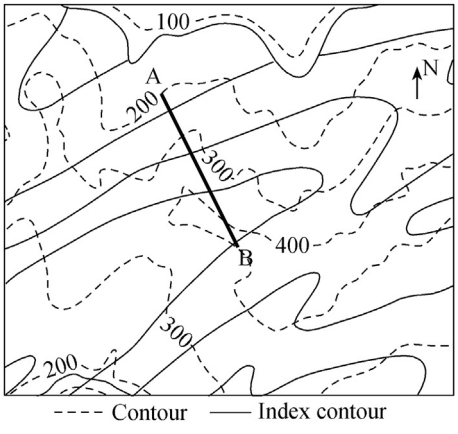

Fig. 3. Elevation contour of study area (units: m).

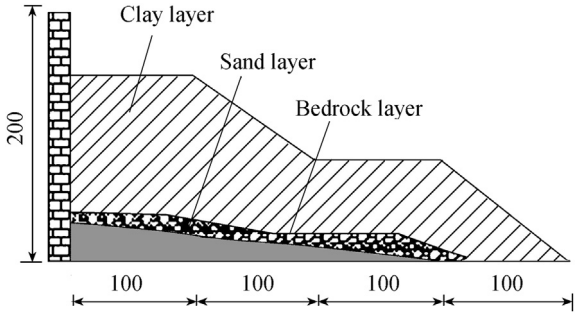

Fig. 4. Stratums of slope model (units: cm).

3.2. Detection system

The detection system was connected to eight TDR soil moisture probes, of the type CS635. Each probe was 15.0 cm long, the diameter was 0.318 cm, and the size was 5.75 cm × 4.0 cm × 1.25 cm. The probe resistance changed with the increase of the dielectric permittivity of soils (Mojid and Cho, 2004; Wraith et al., 2005). Fig. 4 shows the stratums of the slope model with two platforms. The lower part of the slope model was taken as the research object for simulation of slope sliding and debris flow evolution because the flow of mud, the amount of water collection, and the erosion intensity of this part were greater than those of the other part. Fig. 5 shows the side and top views of monitoring points in the lower part of the slope model. The probes were embedded in two layers, 10 cm and 25 cm from the soil surface.

The strain sensors were arranged along the slope on both sides of the axis of the slope surface. They were labeled A and B from right to left (Fig. 6). The sensor detected the deformation by measuring the friction when sliding occurred. Through treatment of collected data, the deformation was transformed into the strain (Cataldo et al., 2014).

After scaling, mechanical properties of soil at corresponding locations in the study area were tested. Fig. 7 shows that shear strengths of the undisturbed soil in the upper layer are greater than those in the lower layer. It can also be reasonably concluded that the shear strength of experimental soil is close to that of undisturbed soil.

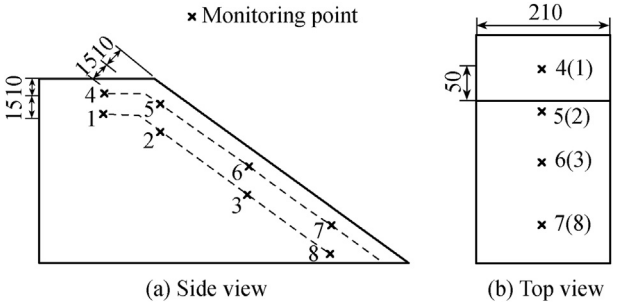

Fig. 5. Views of monitoring points in lower part of slope model (units: cm).

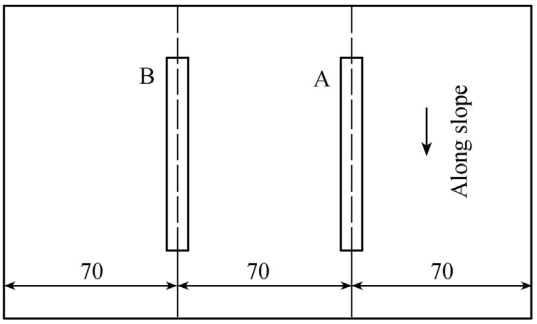

Fig. 6. Positions of sensor ST350 (units: cm).

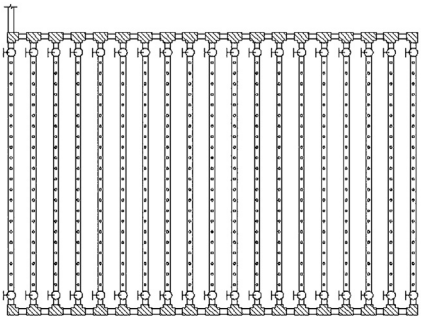

Fig. 8. Structure of rainfall pipes.

3.3. Rainfall generation

The rainfall control system, as shown in Fig. 8, is meant to simulate the rainfall process with different intensity levels. The main system was made of 19 PPR pressure pipes with a diameter of 20 mm. They were parallel to each other with a uniform space of 10 cm and connected by joints-tees. Each of the pipes was mounted with a spraying unit and arranged with a certain number of holes with a uniform space of 1 mm. Two ball valves were also installed on each pipe to control rainfall.

4. Result analysis

The experiment consisted of two phases: the first phase was rainfall-induced landslides and the occurrence of debris flow, and the second phase was the evolution of the debris flow.

4.1. Analysis of soil moisture content after rainfall

During the first phase, the comparative trials with different slopes were divided into four tests, as shown in Table 1. Two rainfall processes with different intensities were simulated in each test, and a duration of 15 min was set between them.

4.1.1. Variation of soil moisture content with time

The curves of the soil moisture content in Fig. 9 show that, in the first stage of different rainfall intensities, the soil moisture content at points in the shallow soil layer (about 10 cm below the slope surface) increases rapidly, with the maximum soil moisture content in the range of 0.30–0.44, and the increase mainly occurs during the latter segment of rainfall. Soil in the deep slope layer, 25 cm below the surface, has a relatively low level of initial soil moisture content because the infiltrated rainwater has not yet reached it. Then, affected by rainwater infiltration, the soil moisture contents at points 1, 2, and 3 in most cases increase quickly, while the shallow soil moisture contents at points 4, 5, 6, and 7 decline. In this stage, the soil moisture content at each point was in a smooth transition state, and slope sliding first occurred in the shallow soil layer along with shallow landslide gullies.

In the second stage of heavy rainfall, the soil moisture content at most points demonstrates its second phase of growth for the steep slope, while, the soil moisture content at the points in the deep soil layer demonstrates that the increasing trend is even more significant for the gentle slope than that for the steep slope. As the rainfall continued, the rainwater gradually penetrated into the deep soil, the violent phenomena of shock and soil slumping began to appear. The slope failure became more severe, and the landslide gradually evolved into debris flow.

As the rainfall stops, the soil moisture contents at different points tend to be constant with time, meaning that the moisture content of the slope soil reaches a stable state.

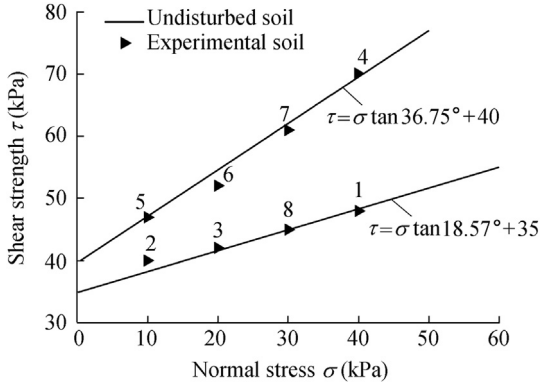

Fig. 7. Comparison of shear strength of undisturbed soil and results at monitoring points in experiment.

4.1.2. Analysis of function of soil moisture content

The numerical simulations reveal that, for the same rainfall event, the variation of soil moisture content is mainly affected by the gradient of slope (β) and depth of soil (h):

Table 1
Rainfall conditions of four tests.

Test	Gradient of slope (°)	First rainfall		Time between rainfalls (min)	Second rainfall	
		Intensity	Lasting time (min)		Intensity	Lasting time (min)
1	40	Heavy	10	15	Heavy	7
2	40	Weak	10	15	Heavy	7
3	30	Weak	10	15	Heavy	7
4	30	Heavy	10	15		

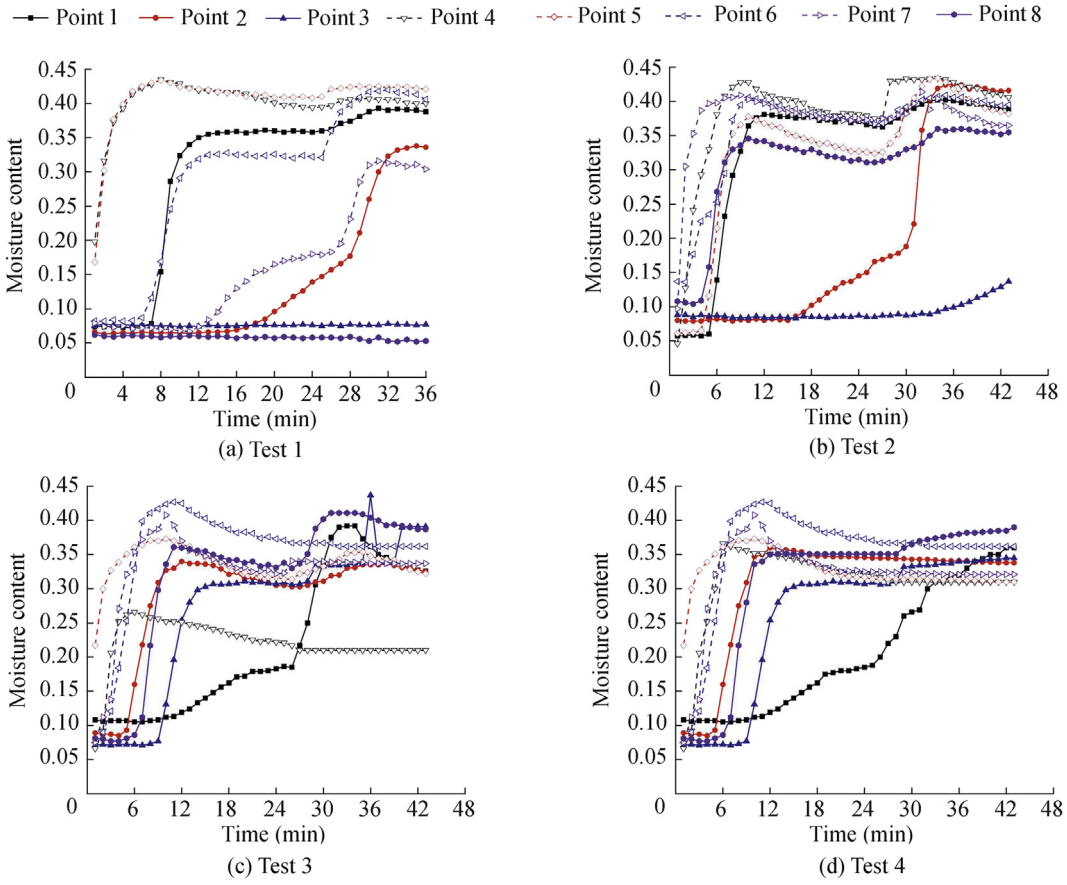

Fig. 9. Soil moisture content curves at different points under different testing conditions.

$$w_t = A_2 + \frac{A_1 - A_2}{1 + (t/x_0)^p} + f(\beta) + g(h) \tag{20}$$

where w_t is the soil moisture content at time t; A_1, A_2, x_0, and p are parameters; and $f(\beta)$ and $g(h)$ are functions of β and h, respectively.

In the examination of the soil moisture content at different depths of soil under the influence of rainfall intensity, shallow soil and deep soil were distinguished by the sliding surface. The soil moisture content above the sliding surface was classified as the shallow soil moisture content (w_{st}), and the soil moisture content under the sliding surface was classified as the deep soil moisture content (w_{dt}). By fitting the experimental results, unified expressions were derived to forecast the soil moisture content at different depths near the sliding surface:

$$w_{st} = 0.36 - \frac{0.25}{1 + (t/3.47)^4} \tag{21}$$

$$w_{dt} = 0.34 - \frac{0.26}{1 + (t/7.5)^7} \tag{22}$$

Fig. 10 shows the fitted results of the soil moisture content. Eqs. (21) and (22) are consistent with the variations of the soil moisture content at corresponding depths.

4.1.3. Effect of growth rate of soil moisture content on slope sliding

Based on the soil moisture content monitoring data, the growth rate of the soil moisture content in deep and shallow soils can be expressed with the same equation:

$$R = \frac{w_{t+\Delta t} - w_t}{w_t} \tag{23}$$

Fig. 11 shows the calculated results regarding the growth rate of the soil moisture content in each group of tests.

As shown in Fig. 11(a), for the steep slope, the soil moisture content rapidly increases at the points near the slope surface during the first heavy rainfall, and the soil moisture content at the point close to the platform increases at an even faster rate, showing that, under the heavy rainfall, variations of the soil moisture content of the steep slope began from the upper slope surface, and grew sequentially along the platform and lower slope surface. As a result, slope sliding first occurred at the upper position of the steep slope during the first heavy rainfall. For the gentle slope, as shown in Fig. 11(d), during the heavy rainfall, the shallow soil moisture content increases rapidly at first, and then the deep soil moisture content increases rapidly after the growth rate of the shallow soil moisture content reaches the peak value. Under such a condition, rainwater infiltrated into the shallow soil over a wide range, and it was highly possible for the gentle

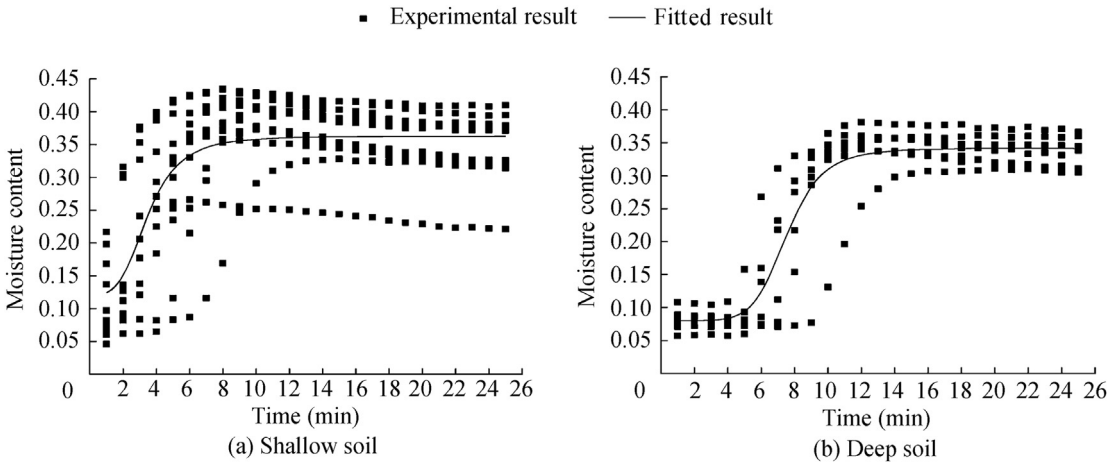

Fig. 10. Variations of soil moisture content at different depths.

slope to slide. In fact, under the heavy rainfall, channels of debris flow developed along the gentle slope, proving the conclusions stated above.

Fig. 11(b) and (c) shows that, after the first weak rainfall, the growth rate of the soil moisture content of the steep slope is larger than that of the gentle slope overall, and that of the gentle slope is significantly affected by the second heavy rainfall. According to the changes in the soil moisture content, failure modes were different for different slopes:

For a steep slope, the runoff velocity was greater than for a gentle slope during the first weak rainfall. In the process, the soil moisture content at the lower part of the slope first increased with the amount of water gathering there (see points 6 and 7), resulting in failure at the lower part of the slope surface, which may cause further destruction.

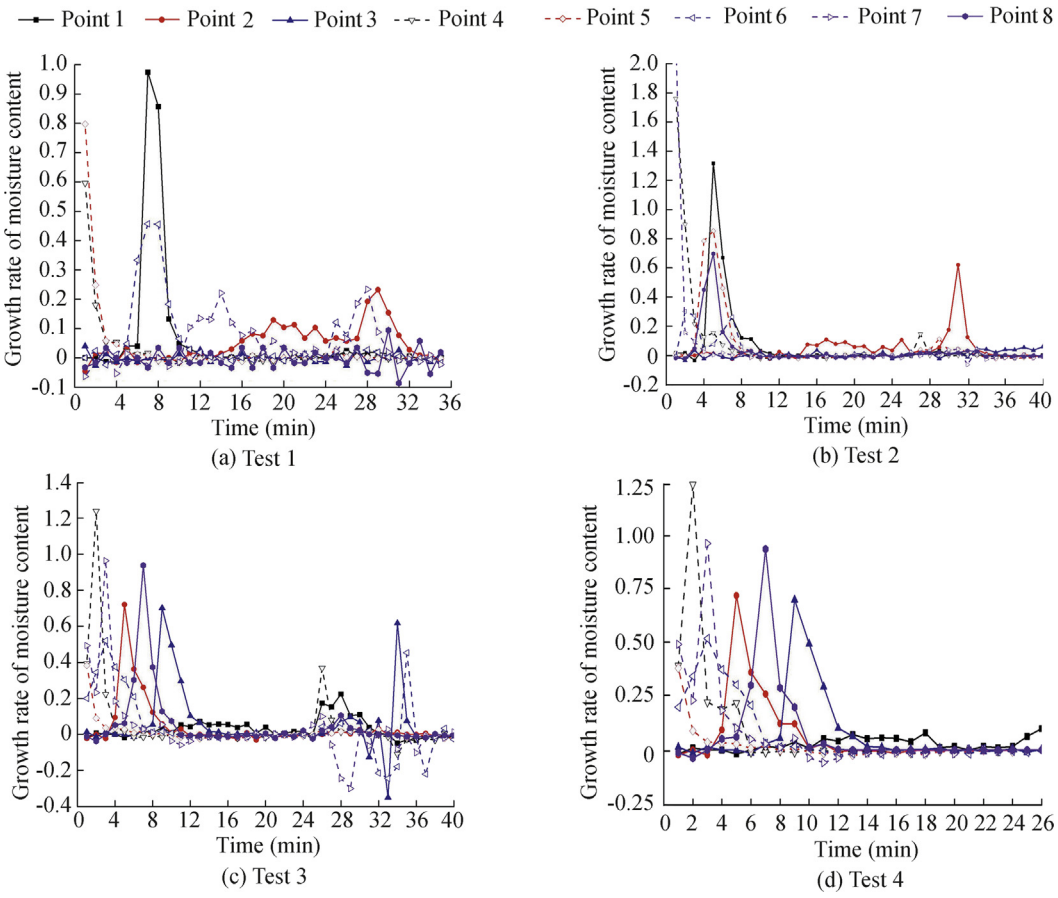

Fig. 11. Curves of growth rate of moisture content at different points.

For a gentle slope, the runoff velocity was low during the first weak rainfall, and it was easier for the rainwater to infiltrate through the slope surface. In this case, several debris flow gullies formed. Thus, at the beginning of the second heavy rainfall, destruction occurred along the gullies. With the continuous rainfall, destruction along the gullies gradually expanded, followed by the evolution of debris flow and the phenomenon of clods slumping.

4.2. Analysis of debris flow evolution

The experiment was performed on a slope with a gradient of 45° and soil density of 2.01 kg/m^3. The major debris flow was considered the research subject in the experimental study. A 30 cm-high barrier was utilized, and each side of it was 30 cm long. It was buried 10 cm deep in the slope soil. Table 2 shows the conditions for different positions and rotation angles of the barrier in the experimental study. l is the length of the slope, and the barrier position means the distance from the barrier to the top platform along the slope.

The experimental and calculated results of the debris flow velocity under four conditions are shown in Fig. 12. In the experiment, the right side of the flow surface was regarded as the research object. Fig. 13 shows the curve of the shear strength of the debris flow.

Fig. 12 shows that, under condition 1, the debris flow is accelerated, and two seconds and four seconds are two significant turning points of the debris flow velocity. The velocity of the debris flow reaches the peak value of 1.6 m/s when it arrives at the slope toe at 4.5 s. Loose materials were carried by the debris flow due to the decreasing shear strength, and the volume of the eroded slope soil increased as well. Under condition 2, the debris flow velocity demonstrated a moderate increase when it came into contacts with the barrier as compared with condition 1 at the same time because the barrier weakened the capacity of the debris flow to carry loose particles. Under condition 3, the barrier diverted the debris flow, leading to a decrease of velocity of 0.1 m/s at 2.5 s. The mass of debris flow was greater on the right side, and the velocity on the right side was significantly higher than that on the other side. As a result, through use of the barrier, the velocity, kinetic energy, and overall shearing force of the debris flow decreased as compared with what they did without use of the barrier, and the severity of soil erosion was lessened.

As shown in Fig. 12, under condition 4, when the barrier was placed at the position of $l/2$, the debris flow maintained its original movement patterns for a relatively long period of time before making contact with the barrier as compared with

Table 2
Positions and rotation angles of barrier set in experimental study.

Condition	Barrier position	Rotation angle (°)
1		0
2	$l/3$	0
3	$l/3$	15
4	$l/2$	0

Note: the rotation angle is obtained by counterclockwise rotation.

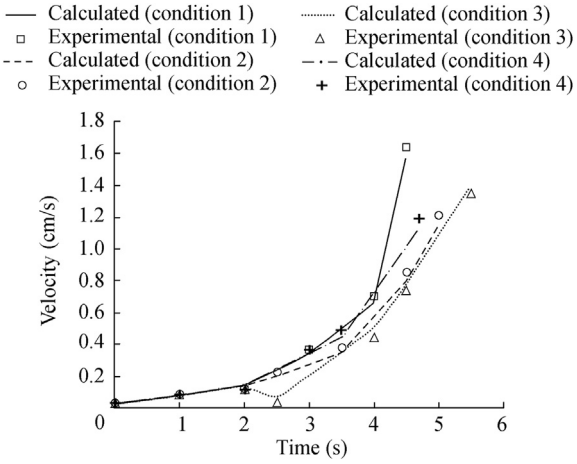

Fig. 12. Curves of debris flow velocity under different conditions.

condition 2. During this period of time, the velocity of the debris flow was the same as that under condition 1, and both velocities were greater than that under condition 2. The velocity of the debris flow reached 0.5 m/s at 3.5 s under condition 4 when it made contact with the barrier, and then the debris flow moved at a newly accelerated pace along the barrier. At this point, the maximum difference between debris flow velocities under conditions 2 and 4 was 0.1 m/s, and, after this, the velocity under condition 4 was greater than that under condition 2. Therefore, the soil erosion in the region of $l/3$ to $l/2$ from the platform under condition 4 was more serious than that under condition 2, which meant that the protective effect of the barrier in the downstream region under condition 4 was weaker than that under condition 2.

Fig. 13 shows that there is a nonlinear negative correlation between the shear strength and time. The shear strength of the debris flow reaches its maximum at one second under four conditions. With the evolution of the debris flow, the number of loose particles increased. In spite of the increasing velocity of the debris flow, the overall shear strength of the slope soil decreased. Especially for the duration from one to three seconds, there was a significant reduction of the shear strength. The curve for condition 1 flattened after four seconds, and the head of the debris flow was close to the slope toe. Along with the worsening liquidity conditions, the overall shear strength was weak and approached the yield stress. With a barrier placed

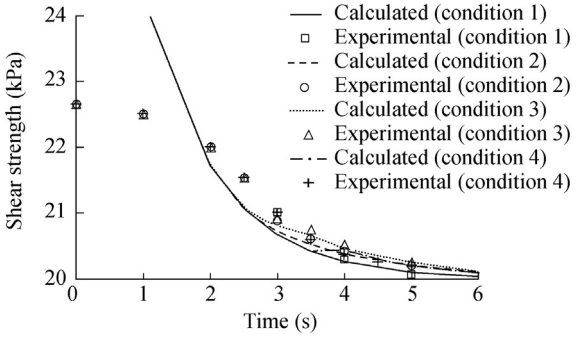

Fig. 13. Curves of shear strength under different conditions.

on the slope surface at the position of *l*/3 from the platform under conditions 2 and 3, the acceleration of the debris flow decreased after 2.0 s, as compared with that under condition 1. The overall shearing force declined and flattened out after five seconds and six seconds, respectively, and remained constant with the value close to the yield stress. The curve of the shear strength under condition 3 is gentler than that under condition 2 because of the influence of the rotation angle of the barrier. The overall energy consumption of the debris flow under condition 3 was larger, the overall shear strength decreased, and the ability of the debris flow to carry loose particles along the slope was relatively weak, leading to the weakened erosion. Under the influence of velocity and mass, total reduction of the shearing force under condition 3 was less than under condition 2 during the evolution of debris flow. Therefore, variations of the shear strength under condition 3 were moderate. Although there is a certain difference between the calculated results and measured data, the overall trends are similar, and the difference is mainly caused by the fact that the deduced formulas are suitable only for the debris flow in the fluid state.

5. Conclusions

In this study, variations of the soil moisture content and shear strength, as well as their relationships with rainfall intensity and slope gradient were obtained, and variations of the velocity of debris flow were also deduced during its evolution. The main conclusions are as follows:

(1) With the occurrence of rainfall, the moisture content of the shallow soil layer increases faster than that of the deep soil layer. As the shallow soil reaches the saturated state, the deep soil moisture content will increase rapidly, meaning that slope sliding first occurs in the shallow soil layer with the occurrence of shallow landslide gullies. As the rainfall stops, soil moisture contents at different points concentrate at certain values, meaning that the moisture content of the slope soil reaches a stable state.

(2) During the process of rainfall, the variation of the soil moisture content at the same depth varies with the slope gradient and rainfall intensity. Under the first heavy rainfall, the variation of the soil moisture content of the steep slope begins from the upper slope surface, and the soil moisture content grows sequentially along the platform and lower slope surface, demonstrating that slope sliding first occurs at the upper position of the steep slope under such a condition. Meanwhile, under the first weak rainfall, changes of the soil moisture content of the steep slope are significant overall, and the soil moisture content at the lower part of the slope first increases because of the high runoff velocity, where relatively serious failure may occur.

(3) Debris flow accelerates with an initial velocity as it flows down along the slope, and loose materials are carried by the debris flow because of the decrease of the shear strength along the slope surface. The impact of the debris flow on the slope soil increases with the ever-increasing mass of the debris flow.

(4) A barrier placed on the slope surface separates and blocks the debris flow. The installation of a barrier at a high position, rotating clockwise at a certain degree, has a better effect on reducing the rainfall-induced slope soil erosion and the destruction caused by debris flow evolution.

Acknowledgements

We are grateful to Professor Matthew Yen at California State University, Fresno, for his advice and selfless help in the modification of this paper.

References

Brighenti, R., Segalini, A., Ferrerob, A.M., 2013. Debris flow hazard mitigation: a simplified analytical model for the design of flexible barriers. Comput. Geotech. 54 (10), 1−15. http://dx.doi.org/10.1016/j. compgeo.2013.05.010.

Cataldo, A., Persico, R., Leucci, G., de Benedetto, E., Cannazza, G., Matera, L., de Giorgi, L., 2014. Time domain reflectometry, ground penetrating radar and electrical resistivity tomography: a comparative analysis of alternative approaches for leak detection in underground pipes. NDT E Int. 62 (3), 14−28. http://dx.doi.org/10.1016/j.ndteint.2013.10.007.

Chen, R.P., Xu, W., Chen, Y.M., 2009. Measuring dielectric constant in highly conductive soils based on surface reflection coefficients. J. Geotech. Geoenviron. Eng. 135 (12), 1883−1891. http://dx.doi.org/10.1061/(ASCE)GT.1943-5606.0000170.

Dowding, C.H., Pierce, C.E., 1994. Measurement of localized failure planes in soil with time domain reflectometry. In: Proceedings, Symposium and Workshop on Time Domain Reflectometry in Environmental, Infrastructure, and Mining Applications. US Department of Interior Bureau of Mines, Minneapolis.

Gartner, J.E., Cannon, S.H., Santib, P.M., 2014. Empirical models for predicting volumes of sediment deposited by debris flows and sediment-laden floods in the transverse ranges of southern California. Eng. Geol. 176 (24), 45−56. http://dx.doi.org/10.1016/j.enggeo.2014.04.008.

Han, Y.S., Liang, C., Han, J., Huang, P., Li, L.W., Peng, S.G., 2012. Gravitation erosion in afflicted areas and its effects of sediment yield and transportation: a case study in Niujuangou Gully. J. Sichuan Univ. (Eng. Sci. Ed.) 44 (s2), 110−116 (in Chinese).

Hottan, N., Ohta, T., 2000. Pore-water pressure of debris flows. Phys. Chem. Earth Ser. B 25 (4), 381−385. http://dx.doi.org/10.1016/S1464-1909(00)00030-7.

Legros, F., 2002. The mobility of long-runout landslides. Eng. Geol. 63 (3−4), 301−331. http://dx.doi.org/10.1016/S0013-7952(01)00090-4.

Liang, Z.G., Chen, Y.M., Chen, R.P., Chen, Y., 2005. Study on applications of coaxial-cable electromagnetic wave reflection technique in monitoring slope stability. Chin. J. Geotech. Eng. 27 (4), 453−458. http://dx.doi.org/10.3321/j.issn.1000-4548.2005.04.018 (in Chinese).

Magnus, B., Oliver, S., 2012. Combining airborne and terrestrial laser scanning for quantifying erosion and deposition by a debris flow event. Geomorphology 138 (1), 49−60. http://dx.doi.org/10.1016/j.geomorph.2011.08.024.

Mancarella, D., Doglioni, A., Simeone, V., 2012. On capillary barrier effects and debris slide triggering in unsaturated layered covers. Eng. Geol. 147−148 (12), 14−27. http://dx.doi.org/10.1016/j.enggeo.2012.07.003.

Mojid, M.A., Cho, H., 2004. Evaluation of the time-domain reflectometry (TDR)-measured composite dielectric constant of root-mixed soils for estimating soil-water content and root density. J. Hydrol. 295 (1−4), 263−275. http://dx.doi.org/10.1016/j.jhydrol.2004.03.012.

Nicholas, T.L., Andrew, J.M., Gordon, E.G., Paul, K., 2014. Debris flow initiation in proglacial gullies on Mount Rainier, Washington. Geomorphology 226 (1), 249−260. http://dx.doi.org/10.1016/j.geomorph.2014.08.003.

Pastuszka, T., Krzyszczak, J., Sławiński, C., Lamorski, K., 2014. Effect of time-domain reflectometry probe location on soil moisture measurement during wetting and drying processes. Measurement 49 (3), 182−186. http://dx.doi.org/10.1016/j.measurement.2013.11.051.

Ragni, L., Berardinelli, A., Cevoli, C., Valli, E., 2012. Assessment of the water content in extra virgin olive oils by time domain reflectometry (TDR) and partial least squares (PLS) regression methods. J. Food Eng. 111 (1), 66−72. http://dx.doi.org/10.1016/j.jfoodeng.2012.01.028.

Robert, C., 2009. Time-domain reflectometry method and its application for measuring moisture content in porous materials: a review. Measurement 42 (3), 329−336. http://dx.doi.org/10.1016/j.measurement.2008.08.011.

Salciarini, D., Tamagnini, C., Conversini, P., 2010. Discrete element modeling of debris-avalanche impact on earthfill barriers. Phys. Chem. Earth A/B/C 35 (3−5), 172−181. http://dx.doi.org/10.1016/j.pce.2009.05.002.

Suits, L.D., Sheahan, T.C., Jonnalagadda, S., Kumar, D., Jain, P., Gawande, N., 2010. Comparison of resistivity and time domain reflectometry sensors for assessing moisture content in bioreactor landfills. Geotech. Test. J. 33 (3), 183−191. http://dx.doi.org/10.1520/GTJ102326.

Wraith, J.M., Robinson, D.A., Jones, S.B., Long, D.S., 2005. Spatially characterizing apparent electrical conductivity and water content of surface soils with time domain reflectometry. Comput. Electron. Agric. 46 (1−3), 239−261. http://dx.doi.org/10.1016/j.compag.2004.11.009.

Yair, A., Klein, M., 1973−1974. The influence of surface properties on flow and erosion processes on debris covered slopes in an arid area. Catena 1, 1−18. http://dx.doi.org/10.1016/S0341-8162(73)80002-5.